Microtubule nucleation remote from centrosomes may explain how asters span large cells

Keisuke Ishihara[a,b,1], Phuong A. Nguyen[a,b], Aaron C. Groen[a,b], Christine M. Field[a,b], and Timothy J. Mitchison[a,b,1]

[a]Department of Systems Biology, Harvard Medical School, Boston, MA 02115; and [b]Marine Biological Laboratory, Woods Hole, MA 02543

This contribution is part of the special series of Inaugural Articles by members of the National Academy of Sciences elected in 2014.

Edited by Ronald D. Vale, Howard Hughes Medical Institute and University of California, San Francisco, CA, and approved November 13, 2014 (received for review October 6, 2014)

A major challenge in cell biology is to understand how nanometer-sized molecules can organize micrometer-sized cells in space and time. One solution in many animal cells is a radial array of microtubules called an aster, which is nucleated by a central organizing center and spans the entire cytoplasm. Frog (here *Xenopus laevis*) embryos are more than 1 mm in diameter and divide with a defined geometry every 30 min. Like smaller cells, they are organized by asters, which grow, interact, and move to precisely position the cleavage planes. It has been unclear whether asters grow to fill the enormous egg by the same mechanism used in smaller somatic cells, or whether special mechanisms are required. We addressed this question by imaging growing asters in a cell-free system derived from eggs, where asters grew to hundreds of microns in diameter. By tracking marks on the lattice, we found that microtubules could slide outward, but this was not essential for rapid aster growth. Polymer treadmilling did not occur. By measuring the number and positions of microtubule ends over time, we found that most microtubules were nucleated away from the centrosome and that interphase egg cytoplasm supported spontaneous nucleation after a time lag. We propose that aster growth is initiated by centrosomes but that asters grow by propagating a wave of microtubule nucleation stimulated by the presence of preexisting microtubules.

aster | centrosome | microtubule nucleation | embryo | *Xenopus*

The large cells in early vertebrate embryos are organized by radial arrays of microtubules called asters. This general organization was described by early cytologists (1) but is clearly illustrated by modern fixed immunofluorescence or live imaging. At the end of mitosis, a pair of asters is observed at the spindle poles but remains small in radius, presumably because cyclin-dependent kinase 1 (Cdk1) inhibits aster growth (2). Once the cell enters interphase, the asters grow at rates of 30 μm/min in *Xenopus* zygotes and 15 μm/min in zebrafish, while maintaining a high density of microtubules at their periphery (2–4). Paired asters interact at the cell's midplane to form a specialized zone of microtubule overlaps, which in turn recruit cytokinesis factors to the cell cortex (5, 6). Cell-spanning dimensions are presumably required so that the microtubules can touch the cortex to accurately position the cleavage furrow according to cell geometry (3, 7, 8).

In the standard model of aster growth, microtubules are nucleated with their minus-ends anchored at the centrosome (9) and polymerize outward with plus-ends undergoing dynamic instability (10). However, there are several issues in applying this model to a very large cytoplasm (11). Because of the radial geometry, the standard model implies a decrease in microtubule density with increasing radius. In contrast, microtubule density seems to be constant or even increase toward the aster periphery in frog and fish zygotes (3). Furthermore, this radial elongation model predicts that a subset of microtubules spans the entire aster radius, but it is unknown whether such long microtubules exist. We wondered whether additional mechanisms promoted aster growth in large cells, such as microtubule sliding, treadmilling, or nucleation remote from centrosomes.

Previously we developed a cell-free system to reconstitute cleavage furrow signaling where growing asters interacted (5, 12). Here, we combine cell-free reconstitution and quantitative imaging to identify microtubule nucleation away from the centrosome as the key biophysical mechanism underlying aster growth. We propose that aster growth in large cells should be understood as a spatial propagation of microtubule-stimulated microtubule nucleation.

Results

Reconstitution of Large Asters in a Cell-Free System. To study aster growth, we used extracts made from unfertilized frog eggs (13) and added calcium immediately before imaging to initiate the interphase cell cycle (12). These extracts are essentially undiluted cytoplasm and support the growth and interaction of large asters that reconstitute spatially organized signaling characteristic of cytokinesis in zygotes (Fig. 1*A* and ref. 5). In most experiments, asters were nucleated with beads coated with activating antibody to Aurora kinase A (AurkA) (14). This kinase plays a key role in microtubule nucleation. The beads mimic centrosomes and lead to similar aster growth as the physiological nucleation site, a pair of centrosomes attached to sperm chromatin (Fig. S1*A*). However, unlike demembranated sperm, the beads provide a point-like center to the aster and facilitate image analysis by avoiding chromatin-mediated nucleation and splitting of the centrosome pair.

At higher bead densities, asters interact, which mutually inhibits further growth (Fig. 1*A* and ref. 5). At low bead density,

Significance

How the cell cytoplasm is spatially organized is of fundamental interest. In ordinary animal cells the cytoplasm is organized by a radial array of microtubules, called an aster. Aster microtubules are nucleated by the centrosome and elongate to the periphery. We investigated how asters grow in an extremely large cell, the frog egg, using microscopy of an extract system. Asters were initially nucleated at centrosomes, but then additional microtubules nucleated far from the centrosome, apparently stimulated by preexisting microtubules. The resulting growth process allows asters to scale to the size of huge egg cells while maintaining a high density of microtubules at the periphery. Microtubule-stimulated microtubule nucleation might be a general principle for organizing large cells.

Author contributions: K.I. and T.J.M. designed research; K.I., P.A.N., A.C.G., and C.M.F. performed research; K.I., P.A.N., A.C.G., and C.M.F. contributed new reagents/analytic tools; K.I. analyzed data; and K.I. and T.J.M. wrote the paper.

The authors declare no conflict of interest.

[1]To whom correspondence may be addressed. Email: kishihar@fas.harvard.edu or timothy_mitchison@hms.harvard.edu.

This article contains supporting information online at www.pnas.org/lookup/suppl/doi:10.1073/pnas.1418796111/-/DCSupplemental.

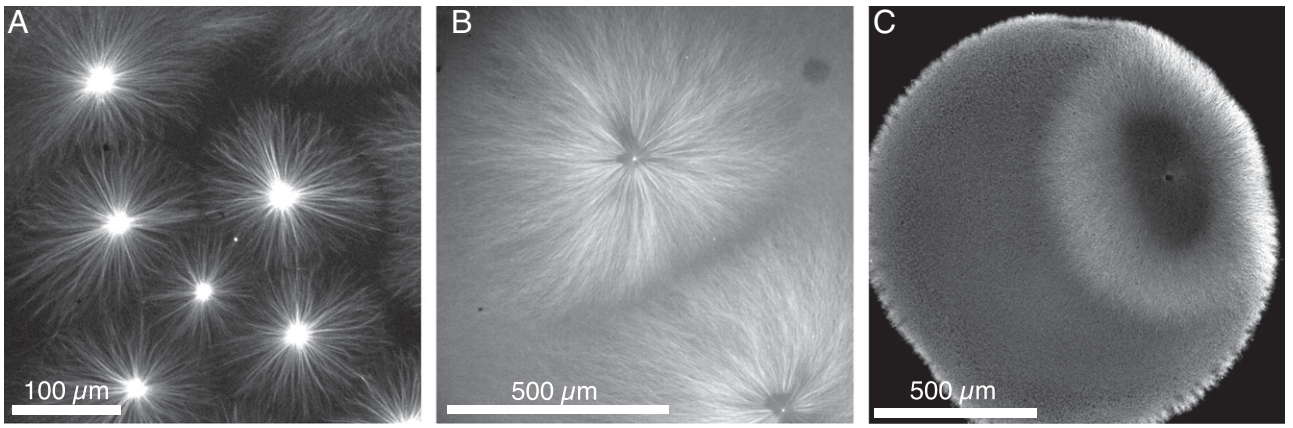

Fig. 1. Reconstitution of large microtubule asters in a cell-free system. (*A*) High density of beads coated with AurkA antibody in interphase *Xenopus* egg extract nucleate many asters that mutually inhibit their growth upon contact, leading to limited radii; 34 min after calcium addition. (*B*) At low bead densities, asters are spatially separated and grow in an uninterrupted manner. Large asters spanning ~500 μm in radius are observed; 45 min after calcium addition. Wide-field images of fluorescently labeled tubulin. (*C*) Asters grow and eventually span the entire cytoplasm of *Xenopus laevis* zygote. Laser scanning confocal images of eggs fixed at 45 min after fertilization and stained for tubulin by immunofluorescence.

we observed assembly of asters as large as those observed in vivo, spanning 500 μm or more in radius (Fig. 1 *B* and *C*). Aster radius grew continuously for 30–80 min after addition of calcium. At later time points, microtubules often appeared spontaneously in the cytoplasm, which interfered with further aster growth (Fig. S1*B*). The centers of asters in extract usually did not show a drastic loss of microtubules, as seen in fixed frog zygotes or live zebrafish embryos (3). We concluded that our cell-free system was capable of reconstituting large asters at length and time scales of aster growth similar to those in frog zygotes, and we decided to use this system to study aster growth mechanisms.

Large Asters Assemble in the Absence of Microtubule Sliding. One biophysical process that might contribute to aster growth is outward microtubule sliding (4, 15). To assess this, we applied fluorescent speckle microscopy (16). Speckles result from random incorporation of a small fraction of labeled tubulin into the microtubule lattice, and can be used as fiduciary marks to

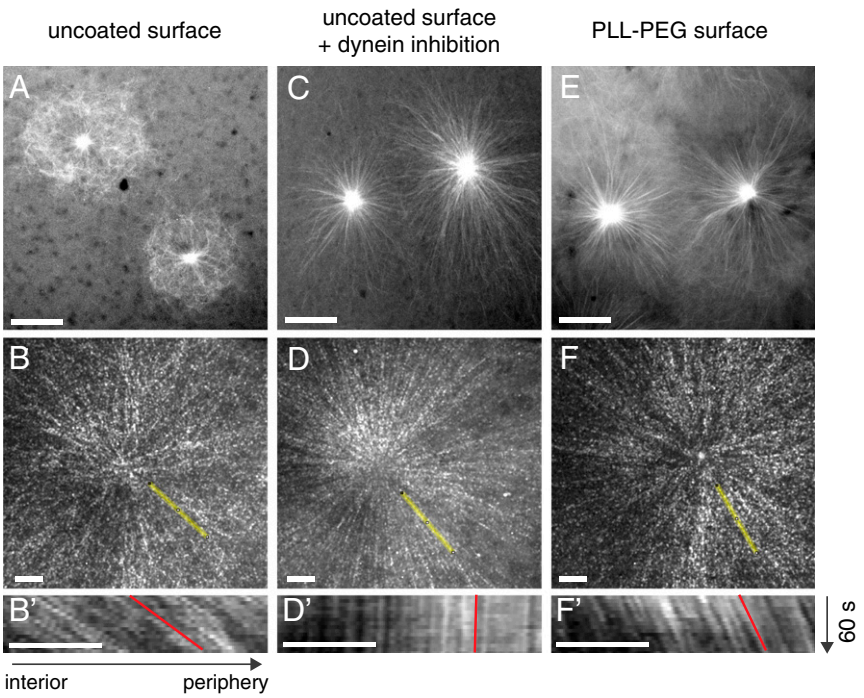

Fig. 2. Large asters assemble in the absence of dynein-mediated microtubule outward sliding. (*A*) Asters assembled between uncoated coverslips show curved and disorganized microtubules. Image acquired on a wide-field microscope; 15 min after calcium addition. (Scale bar, 50 μm.) (*B*) First frame of a fluorescence speckle microscopy movie (Movie S1) showing labeled tubulin in an aster near its center. Image acquired on a spinning disk microscope. Movies were subjected to particle image velocimetry to determine the outward sliding rate as 6.1 ± 2.8 μm/min (SD, n = 12 asters). (Scale bar, 10 μm.) (*B′*) Kymographs generated from yellow line in *B*, where left to right corresponds to interior to periphery of the aster. (Scale bar, 10 μm.) (*C–D′*) Same as *A–B′*, in the presence of p150-CC1 protein to inhibit dynein motor activity. Note the decreased curving of aster microtubules and the complete suppression of microtubule outward sliding, −0.16 ± 0.25 μm/min (n = 12 asters) (Movie S2). (*E–F′*) Same as *A–B′*, with the coverslip surface passivated by PLL-PEG. This also resulted in the decrease of microtubule curving and the reduction of microtubule outward sliding to 2.7 ± 1.2 μm/min (n = 6 asters) (Movie S3).

detect polymer sliding. Speckle movement was quantified using velocimetry software (*Materials and Methods*). To illustrate sliding movement we also show kymographs in Fig. 2. Asters assembled on uncoated glass coverslips exhibited highly curved and disorganized microtubules at their periphery (Fig. 2*A*), and the microtubules slid radially outward at 6.1 ± 2.8 μm/min (SD, $n = 12$ asters) (Fig. 2*B* and Movie S1).

Outward sliding is likely driven by dynein pulling from sites in the cytoplasm and/or coverslip surface (15). One candidate is the minus-end directed motor dynein. When dynein was inhibited by addition of the p150-CC1 fragment of dynactin (17), still on uncoated glass coverslips, microtubules were much more straight and bundled (Fig. 2*C*), and outward sliding was blocked (Fig. 2*D* and Movie S2). Thus, both curving and outward sliding were driven by dynein. Passivating the coverslip surface by adsorption of poly-L-lysine PEG (PLL-PEG) also resulted in loss of most curling (Fig. 2*E*) and decreased outward sliding rate to 2.7 ± 1.2 μm/min (SD, $n = 6$ asters) (Fig. 2*F* and Movie S3). Presumably, surface passivation by PLL-PEG decreased dynein binding to the glass, and this decreased its sliding and curling actions. Despite the varying degrees of microtubule sliding, we observed large asters spanning hundreds of microns in all conditions. In a previous study in zebrafish embryos, dynein perturbation inhibited aster movement but not their growth (3). Taken together, we conclude that outward microtubule sliding can occur in growing asters and might contribute to growth in eggs but is not essential for growth. The effect of microtubule sliding on aster growth rate is discussed below.

Microtubule Treadmilling Does Not Occur During Aster Growth. Another process that could contribute to aster expansion, which speckle microscopy would miss, is outward treadmilling. Polymer treadmilling occurs when one end of a microtubule polymerizes while the other depolymerizes. This would have an effect of increasing microtubule density at the periphery while decreasing it in the interior of the aster. Given the orientation of microtubules in the aster, we would expect outward plus-end polymerization and outward minus-end depolymerization as evidence of treadmilling.

To test this prediction, we performed intensity difference analysis between subsequent frames in tubulin images collected by total internal reflection fluorescence (TIRF) microscopy (Fig. 3*A* and Movie S4). We inhibited microtubule sliding via dynein inhibition and focused on the interior of established asters, where movement of microtubules normal to their axis was minimal. In the images that represent the positive difference between subsequent frames, we observed polymerization (Fig. 3*A*, *Upper Right*, and Movie S5). This morphologically resembled EB1-GFP comets (see below) consistent with a spatial map of microtubule polymerization at their plus-ends. Kymograph analysis suggested outward polymerization rates of 30.0 ± 4.3 μm/min (SD, $n = 56$ ends from four asters) (Fig. 3*B*, *Upper*), in agreement with similarly analyzed EB1 comet velocities 28.2 ± 2.8 μm (SD, $n = 32$ ends). In the images that represent negative difference, we observed shrinkage of microtubules. Here we observed rapid inward movement at 41.8 ± 5.2 μm/min (SD, $n = 50$ ends from four asters) (Fig. 3*A*, *Lower Right*, and Movie S6), presumably corresponding to plus-end depolymerization (Fig. 3*B*, *Lower*). We did not observe outward depolymerization of minus-ends, which would have been the signature of outward treadmilling. In summary, this analysis was most consistent with aster microtubules undergoing classic, two-state dynamic instability on plus-ends and no fast polymerization dynamics on minus-ends.

Quantification of Plus-End Density and Aster Growth Rate. To measure the spatiotemporal distribution of microtubule plus-ends during aster growth, we added EB1-GFP, a microtubule-associated protein that tracks growing plus-ends as bright comets (18), and quantified them by image analysis. Every 2 min, a single

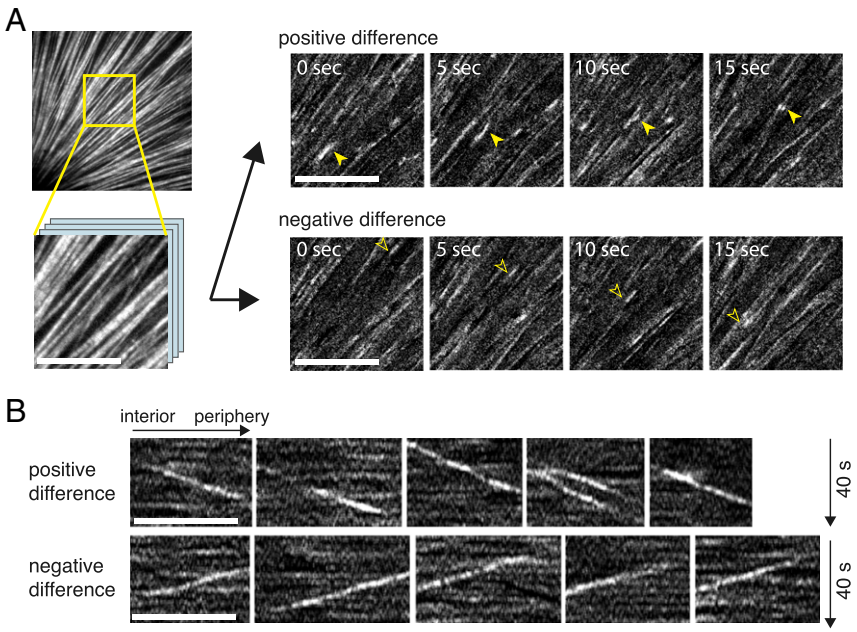

Fig. 3. Tubulin intensity difference imaging reveals dynamic microtubule plus-ends in a growing aster. (*A*) Microtubules were imaged with labeled tubulin by TIRF microscopy (Movie S4). To facilitate analysis of polymer dynamics, intensity differences of subsequent images were calculated to yield maps of polymerization (positive difference; Movie S5) and depolymerization (negative difference; Movie S6) (*Materials and Methods*) (Scale bars, 10 μm.) (*B*) Kymographs were constructed to measure the rates of polymerization and depolymerization observed above. Polymerization proceeded outward at 30.0 ± 4.3 μm/min (SD, $n = 56$ ends from four asters), whereas depolymerization traveled inward at 41.8 ± 5.2 μm/min (SD, $n = 50$ ends from four asters), representing plus-end dynamics. (Scale bars, 10 μm.)

image of labeled tubulin was acquired, followed by four images of EB1-GFP at 3-s intervals (Fig. 4*A*). An automated image analysis procedure (19) tracked plus-end growth rate and direction, and most important for this study, counted the number of EB1 comets found at a given distance from the center of the aster. In this way we obtained a quantitative description of aster growth in terms of total EB1 comet number (Fig. 4*B*) and density (Fig. 4*C*). Compared with tubulin fluorescence intensity, which suffers from low signal-to-noise, EB1 counting is a sensitive method for detecting microtubules (Fig. 4*A*, *Insets*). We determined the aster edge as the half-maximum position of the EB1 comet distribution curves (Fig. 4*B*) at different time points. This analysis showed that aster radius increased linearly at a constant rate (Fig. 4*B*, *Inset*). We quantified the growth rate of aster radius as 29.0 ± 2.9 μm/min (SD, $n = 5$ asters) in the presence of dynein-mediated microtubule outward sliding (EB1 density plots in Fig. S2*A*) and 22.0 ± 4.1 μm/min (SD, $n = 9$ asters) with dynein inhibition. As expected, dynein-mediated outward sliding of microtubules accelerated aster growth rate (Fig. S2*B*). These radial expansion rates are comparable to the estimated 25–30 μm/min aster growth rates in frog embryos (3).

In the radial elongation model with constant microtubule nucleation from the centrosome, we would expect a spatial dilution of EB1 comets with increasing distance from the center.

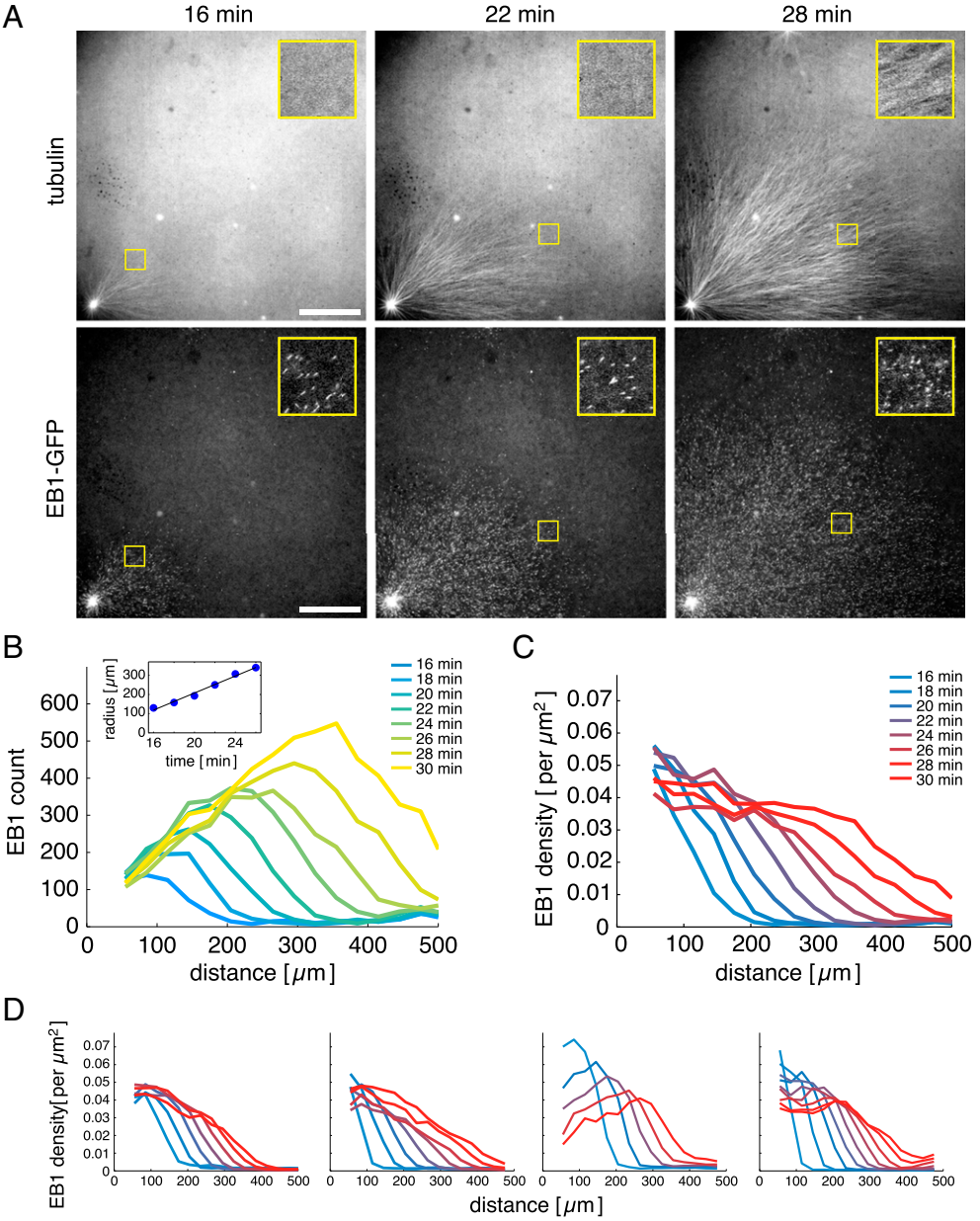

Fig. 4. Quantification of microtubule plus-ends during aster growth. (*A*) Live imaging of labeled tubulin and the plus-end tracking protein EB1-GFP using wide-field microscopy. Images show dynein-inhibited asters assembled under PLL-PEG passivated coverslips. (*Insets*) Magnification of region in yellow box. Time indicates time after calcium addition. (Scale bars, 100 μm.) (*B*) Time evolution of the number of EB1 comets detected at a given distance. Comets were detected and tracked using the PlusTipTracker software (19) (*Materials and Methods*). (*Inset*) Half-maximum positions of the EB1 comet number at different time points. (*C*) Time evolution of the EB1 comet density at a given distance. (*D*) Gallery showing the EB1 density of multiple examples of aster growth. Curves in each plot are 2 min apart.

However, an increasing number of EB1 comets appear with aster growth (Fig. 4*B*), and the comet density was fairly uniform away from the AurkA bead at 0.03–0.04 per μm^2 (Fig. 4*C*). The focal plane with a 20× 0.75 N.A. objective is ∼2 μm deep in z, and most EB1 comets were concentrated at a single focal plane using PLL-PEG passivated coverslips. Assuming a sample thickness of ∼10 μm, we can extrapolate a volume density of 0.006–0.008 growing plus-ends per μm^3, but this value is only an estimate. Our quantitative measurements of reconstituted asters show that microtubules are not spatially diluted in the radial geometry and strongly suggest that new microtubule ends are generated in the aster at locations far away from the organizing center.

Plus-Ends Are Generated at Locations Far from AurkA Beads During Aster Growth. To estimate what fraction of the microtubules in an aster originate from our centrosome mimic, the AurkA beads, we counted the number of tracks that crossed a circle of radius 40 μm away from the bead (Fig. 5*A*) where EB1 comets stayed in a single focal plane, allowing for reliable tracking (Fig. 5*A*'). This radius was chosen arbitrarily, but the analysis is not very sensitive to it (Fig. 5*B*). We estimated the nucleation rate from AurkA beads as 62 ± 17 microtubules per min (SD, $n = 8$ time points) in an imaged quadrant, or ∼250 per min in the whole aster. This rate stayed constant over ∼30 min in some asters (Fig. 5*B*) and extract preparations, whereas in others, the rate gradually decreased, and the center of the aster slowly hollowed out. The EB1 comet densities of examples with and without hollowing are shown in Fig. 4*D*. Fig. 5*B* shows nucleation rate from the AurkA bead over time, determined as in Fig. 5*A*', which was fairly constant in this example. Fig. 5*C* shows total EB1 comet number over time in the whole quadrant (blue circles) and the time-integrated contribution from bead nucleation (red crosses). Comparison of these two plots reveals that the fraction of total growing plus-ends within an aster due to nucleation from the bead decreases over time, as nucleation away from the bead starts to dominate (Fig. 5*C*, *Inset*). Analysis of multiple asters (Fig. S3) led us to conclude that that our centrosome mimic, the AurkA bead, contributes at most 50% of plus-ends to the entire aster during growth, and often far less.

Microtubule Nucleation and Aster Assembly in the Absence of Centrosomes. Our quantitative analysis pointed to a centrosome-independent origin of microtubule ends during aster growth. To directly test the requirement of centrosomes for microtubule nucleation, we imaged interphase extract in the absence of added nucleating templates. Initially, EB1 comets were only sparsely observed in the imaging field, but their number started to increase and quickly reached a saturating density of 0.036 per μm^2 (Fig. 6 *A* and *B*), comparable to the density inside growing asters. The exact timing of spontaneous microtubule assembly was variable, ranging from 20 to 80 min after calcium addition, and seemed to depend on extract preparation, time elapsed since preparation, and position imaged within the sandwiched extract sample. However, the appearance of EB1 comets consistently exhibited sigmoidal kinetics. We did not observe such rapid microtubule assembly with extracts arrested in meiotic metaphase. Thus, spontaneous microtubule assembly seems to be a property specific to the interphase cytoplasm.

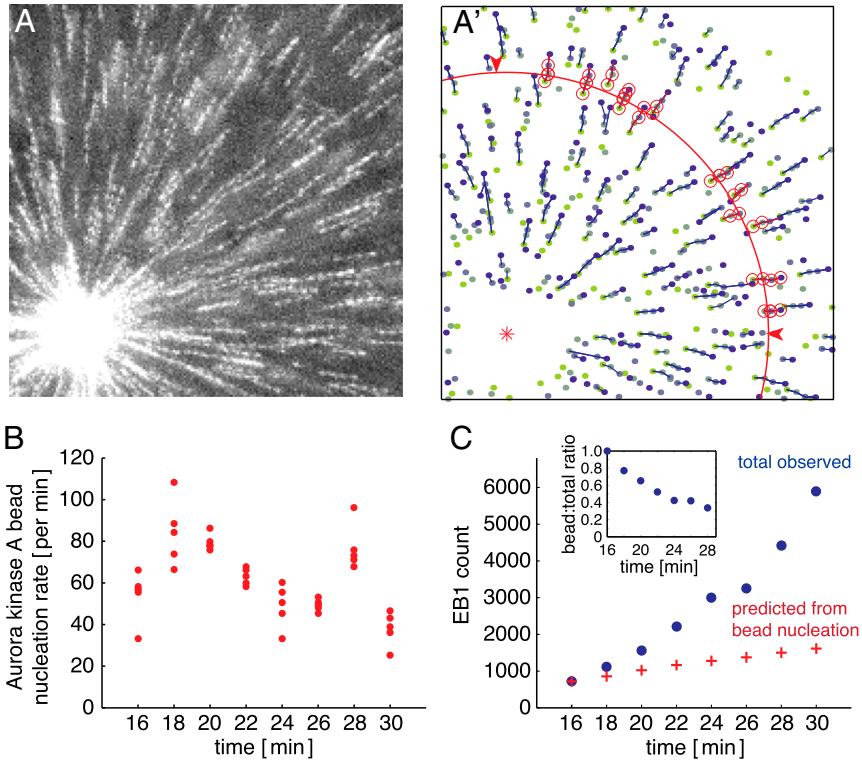

Fig. 5. Microtubules in the aster appear at a distance from the organizing center. (*A*) Maximum intensity projection of four consecutive EB1-GFP images taken over 9.6 s. Same aster as in Fig. 4*A* at 28 min after calcium addition. (*A'*) Particle tracking was applied to the same four images (shown in *A*) to measure microtubule nucleation from AurkA bead (red asterisk). All EB1 comets detected are represented as dots varying from green to blue (frame 1–4). Blue lines represent all detected tracks. Red circles indicate tracks that were detected as crossing the 40-μm perimeter (line). Details in *Materials and Methods*. (*B*) AurkA bead nucleation rate measure as in *A'*. For each time point, number of comets crossing over radii of 38, 39, 40, 41, and 42 μm are shown in the plot. (*C*) Total number of EB1 comets increase dramatically as the aster grows (blue dots). The predicted number of EB1 comets based on the nucleation of AurkA bead alone (red plus signs) is significantly lower. (*Inset*) Ratio of bead (red) to total (blue) at each time point.

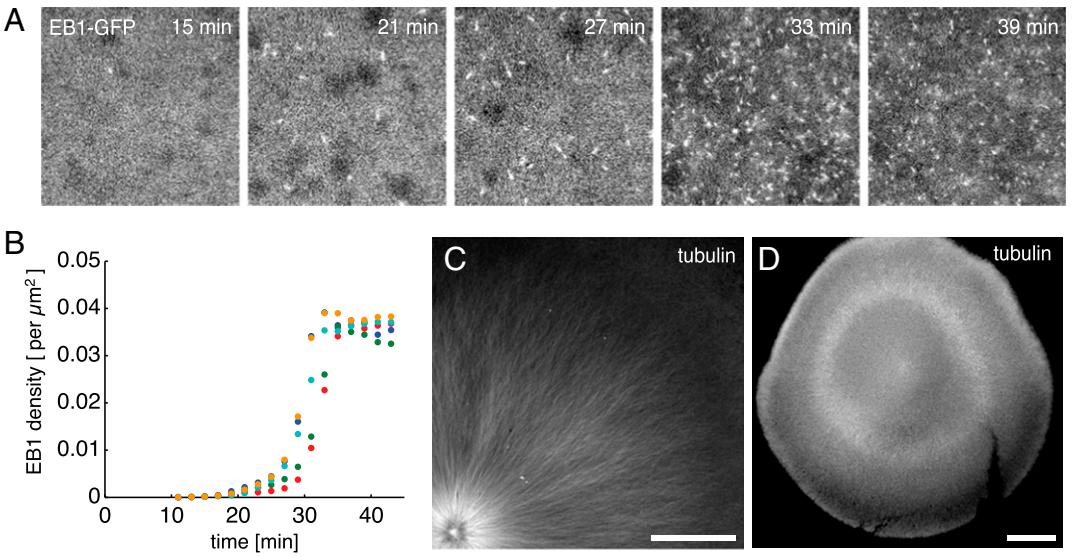

Fig. 6. Microtubules assemble in the interphase cytoplasm in the absence of centrosomes. (*A*) Time lapse image of spontaneously nucleated microtubules in the interphase extract with EB1-GFP. Time denotes time after calcium addition. (*B*) Quantification of EB1 comet density over time for the same reaction as in *A*. Different colors represent different positions of the same coverslip. (*C*) *Tetrahymena* pellicles in interphase extract nucleate microtubules and form large radial arrays of microtubules resembling asters. (Scale bar, 100 μm.) (*D*) Immunofluorescence image showing the pattern of tubulin in eggs fixed at 90 min after electroactivation. (Scale bar, 200 μm.)

To directly test the requirement of centrosomes in the growth of large asters, we introduced *Tetrahymena* pellicles in the interphase extract as microtubule nucleation centers. These provide a large number of basal bodies that can elongate microtubules in extract. Pellicles nucleated large asters with radii spanning hundreds of microns that were morphologically similar to asters assembled by sperm and AurkA beads (Fig. 6*C*), except for a higher microtubule density in the center. Thus, aster growth does not require a special biochemical activity of centrosomes. Finally, we asked whether aster growth occurs in intact frog eggs devoid of centrosomes. To this end we artificially induced eggs to enter the interphase cell cycle by electric shock, fixed and stained for microtubules for immunofluorescence. We observed microtubule patterns resembling asters in some activated eggs (Fig. 6*D*), in agreement with previous reports (20, 21). Thus, even in the absence of centrosomes, microtubule asters form and span the large interphase cytoplasm of frog eggs.

Discussion

In this study we set out to elucidate the biophysical mechanisms underlying the growth of large microtubule asters in large embryonic cells. We first showed that microtubule sliding (Fig. 2) and treadmilling (Fig. 3) are not essential to this process, although dynein-driven outward sliding can contribute to the radial expansion rate (Fig. S2). By developing an assay for the quantification of growing plus-end number (Fig. 4) and nucleation rate from the organizing center (Fig. 5), to our knowledge we have provided the first definitive evidence for the generation of new microtubule plus-ends away from the centrosome during aster growth. Importantly, new microtubule ends were preferentially generated within growing asters, but they eventually assembled even in the absence of nucleating templates (Fig. 6). Three distinct mechanisms might explain preferential nucleation within growing asters: (*i*) a microtubule-independent signal originating from the centrosome and propagating through the cytoplasm, which in turn locally instructs microtubule nucleation; (*ii*) severing of preexisting microtubules in the aster; and (*iii*) microtubule-stimulated microtubule nucleation occurring in the aster. Mechanism (*i*) seems unlikely because we found large asters to assemble in interphase extract supplemented with pellicles and in electro-activated eggs lacking centrosomes (Fig. 6 *C* and *D*). Mechanism (*ii*) was not supported by any imaging data, and Katanin, the dominant microtubule-severing enzyme in *Xenopus* egg extract, is known to be inactive in interphase (22, 23). The sigmoidal kinetics of spontaneous microtubule assembly (Fig. 6*B*) is consistent with microtubule self-amplification, although other mechanisms could also explain this observation, such as a time-dependent decrease in Cdk1 phosphorylation sites (12, 24) that eventually allows nucleation. To simultaneously explain our observations of aster growth and spontaneous microtubule assembly, we favor a mechanism whereby microtubule nucleation is locally promoted by preexisting microtubules in the aster.

In contrast to mitotic spindles that are limited in size (2), interphase asters seem to grow in an unbounded manner. In the fish and frog zygotes, asters grow continuously until they contact another aster or the cell cortex (3). In the extract system, aster growth is halted by contact with a neighboring aster (5, 6) or with spontaneous microtubules that appear in the background at later time points (Fig. S1*B*). It is of interest whether individual microtubules that compose the unbounded aster are themselves bounded or unbounded in length. In theory, this is determined by the precise dynamics of microtubule plus-ends: if the time-weighted average of polymerization and depolymerization is positive (i.e., net polymerization), microtubules are unbounded in length. If the average is negative, all plus-ends eventually shrink back to their minus-ends (i.e., net depolymerization) and are replaced by newly nucleated ones. Previous work suggested bounded growth in mitosis and unbounded in interphase (25). Our EB1 and tubulin images suggest the existence of approximately steady-state conditions for both total microtubule density and total growing plus-end density in the aster interior. This implies that the growth of individual microtubules is bounded, at least in the aster interior. If it was unbounded, either the total microtubule density would have to increase continually, which would be evident in tubulin images, or the plus-end density would have to decrease significantly, which was usually not observed (Fig. 4*D*). We propose that individual microtubules are bounded in length but self-amplifying nucleation promotes the

aster growth in an unbounded manner to span the millimeter-sized cytoplasm. How microtubule dynamics and nucleation contribute to aster growth rate and microtubule density is an important topic for future studies.

In summary, we propose a two-step model of aster growth in large embryonic cells (Fig. 7). Aster growth is initiated by AurkA-dependent microtubule nucleation at the centrosome, but the length of these microtubules is bounded by the dynamic instability of plus-ends. When sufficient local microtubule density builds up, or perhaps when Cdk1 site phosphorylation drops below some threshold, aster growth transitions to a phase in which microtubule-stimulated microtubule nucleation promotes expansion of the aster periphery while maintaining high microtubule density. Local initiation coupled with a signal-amplification mechanism has been highlighted as an important design principle underlying the mitotic trigger waves that coordinate the large cytoplasm of frog eggs (11, 26). Similarly, our model of aster growth views the interphase cytoplasm as an excitable system for microtubule assembly. In contrast to the cell cycle oscillator whose molecular components and dynamics have been well studied, much less is known about microtubule nucleation and how it may be regulated by preexisting microtubules (27–30). Studying aster growth as an emergent property of microtubules may allow us to address these outstanding issues.

Materials and Methods

Aster Reconstitution in *Xenopus* Egg Extract. *Xenopus* egg extract was prepared and interphase asters were assembled using Protein A Dynabeads (Life Technologies) coated with AurkA antibody as previously described (5, 12). Addition of the actin depolymerizing drug cytochalasin D had no noticeable effect on aster growth, and the majority of data presented in this study omitted it. EB1-GFP was purified as in ref. 31 and used at a final concentration of 60 nM. For dynein inhibition, the p150-CC1 fragment of dynactin was purified as in ref. 17 and used at a final concentration of 0.04 mg/mL. PLL-PEG was synthesized as in ref. 32 and adsorbed to glass coverslips (cleaned by sequential sonication in 3M KOH solution and ethanol) during a 15-min incubation as a 0.01-mg/mL solution in 10 mM K-Hepes (pH 7.8) buffer. *Tetrahymena* pellicles were a gift from Jan Brugues, MPI-CBG, Dresden, Germany.

Fluorescent Speckle Microscopy and Velocimetry. Alexa 647-labeled bovine tubulin was used at a final concentration of ~5 nM, which corresponds to ~1:4,000 of tubulin dimers being labeled in the extract. A Nikon E800 upright microscope equipped with a 60× Plan Apo 1.40 N.A. objective lens (Nikon), a Yokogawa CSU10 spinning disk (Perkin-Elmer), a cooled CCD camera (Hamamatsu ORCA-ER), and Melles Griot Krypton/Argon ion laser (488 nm, 568 nm, 647 nm) was driven by Metamorph (Molecular Devices). Aster centers were positioned in the center of the field, and images were captured at 4-s intervals with 2 × 2 spatial binning mode. Microtubule sliding was quantified using a particle imaging velocimetry plug-in for ImageJ (33). Movement was projected to the radially outward vector and spatially averaged for each movie.

Tubulin Intensity Difference Analysis. Dynein-inhibited asters were assembled under coverslips treated with κ-casein (5, 12). This passivation reduced surface binding of unincorporated, labeled tubulin, while still allowing for microtubules to attach to the coverslip. TIRF microscopy was performed on a Nikon Ti-E motorized inverted microscope equipped with a Nikon motorized TIRF illuminator, Perfect Focus, a Prior Proscan II motorized stage, Agilent MLC400B laser launch (488 nm, 561 nm, 647 nm), and an Andor DU-897 EM-CCD camera. Alexa 647-labeled bovine tubulin was imaged with a 100× CFI Apo 1.49 N.A. TIRF objective lens (Nikon) coupled with 1.5× tube lens. Stream acquisition of images at 500-ms intervals was performed using the RAM capture mode in NIS-Elements software (Nikon Instruments) to yield Movie S4. ImageJ software (34) was used to construct intensity difference images. Because the difference of raw fluorescence intensities was dominated by the gradual photobleaching of the fluorophore, we normalized the signal in each frame before image subtraction. The differences of images that were four frames apart yielded the best signal to noise ratio. Finally, a rolling average filter of four frames was applied to yield Movies S5 and S6. The resultant movies were used to construct kymographs in ImageJ.

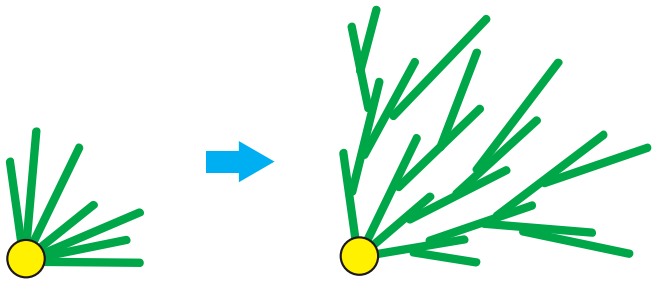

Fig. 7. A two-step model for large aster growth. At early time points, aster growth is initiated by AurkA-dependent microtubule nucleation at the centrosome. Later in interphase, aster growth is sustained by microtubule nucleation away from the centrosome, presumably stimulated by preexisting microtubules.

Quantification of EB1 Comets and Aster Growth Rate. Wide-field images were acquired on a Nikon Eclipse Ni-E upright microscope at MBL equipped with a CFI Plan Apochromat Lambda 20× 0.75 N.A. objective lens (Nikon), Nikon motorized XY stage, Nikon HG precentered fiber illuminator (Intensilight C-HGFIE), and Hamamatsu ORCA-Flash4.0 LT scientific CMOS camera, driven by NIS-Elements. Every 2 min a single image of labeled tubulin was acquired, followed by four images of EB1-GFP at 3-s intervals. EB1 comets were identified using PlusTipTracker software (19), and their distribution was analyzed with custom code written in MATLAB (MathWorks). Aster growth rate was measured by determining the half-maximum positions of EB1 count as in Fig. 4*B*. Identification of EB1 comets in the absence of nucleating sites was done with the MOSAIC plugin (35) for ImageJ. Some images were acquired on the same setup in which the Andor Neo sCMOS camera was used instead. Images at Harvard Medical School were acquired on a Nikon 90i upright microscope equipped with 20× CFI Plan Apo 0.75NA, a Prior Lumen 200 metal arc lamp, Prior ProScan III motorized XY stage, and Hamamatsu ORCA-ER cooled CCD camera, driven by Metamorph.

Measurement of Microtubule Nucleation from AurkA Beads. The same positional information of EB1 comets identified in the step above was further processed to estimate the nucleation rate from the AurkA beads. We initially found that PlusTipTracker performed poorly in tracking comets with minimal number of frames, but this was overcome by transforming the comet positions from Cartesian to polar coordinates. This transformation adds the prior knowledge that the EB1 comet trajectories are oriented in the radial direction (rather than random) and resulted in successful reconstruction of trajectories (minimum of three EB1 comets) as verified by manual inspection. A custom MATLAB script was used to score comets crossing over a given radius from the bead into the quadrant of interest.

Immunofluorescence Imaging of Frog Eggs. Fertilized eggs were fixed by transfer to 90% (vol/vol) methanol, 50 mM EGTA, processed, and stained as previously described (5). Samples were imaged with a laser scanning confocal microscope from the Nikon Imaging Center at Harvard Medical School. Plan Apo 10× 0.45 N.A. (Nikon) and Plan Fluor 20× 0.75 N.A. (Nikon, with Nikon immersion oil) objective lenses were used on a Nikon Ti-E inverted microscope with a Nikon A1R point scanning confocal head, driven by NIS-Elements. For electrical activation, eggs were squeezed into 1× MMR. The jelly coat was removed by swirling the eggs for ~5 min in 2% (wt/vol) cysteine in 0.2× MMR, pH adjusted to 7.8 with KOH, and then rinsing three times in 0.2× MMR. A horizontal DNA gel box with a bed measuring 8.5 inches from electrode to electrode was filled with 0.2× MMR. De-jellied eggs were placed in a line across the gel box approximately equidistance from both electrodes and shocked with 90 V DC for 1 s. Pigment contraction at the animal pole a few minutes after electrical shock indicated successful activation. Eggs were incubated in 0.2× MMR for 40–90 min at 20 °C until fixation. Eggs were fixed and imaged as described above.

ACKNOWLEDGMENTS. We thank the members of the Mitchison laboratory for helpful discussion; Jan Brugues for providing *Tetrahymena* pellicles; the Nikon Imaging Center at Harvard Medical School; and Lynne Change (Nikon Inc.) at Marine Biological Laboratory for microscopy support. This work was supported by National Institutes of Health Grant GM39565 and by Marine Biological Laboratory summer fellowships. K.I. is supported by the Honjo International Scholarship Foundation.

1. Wilson EB (1925) *The Cell in Development and Inheritance* (Macmillan, New York).
2. Wühr M, et al. (2008) Evidence for an upper limit to mitotic spindle length. *Curr Biol* 18(16):1256–1261.
3. Wühr M, Tan ES, Parker SK, Detrich HW, 3rd, Mitchison TJ (2010) A model for cleavage plane determination in early amphibian and fish embryos. *Curr Biol* 20(22):2040–2045.
4. Wühr M, Dumont S, Groen AC, Needleman DJ, Mitchison TJ (2009) How does a millimeter-sized cell find its center? *Cell Cycle* 8(8):1115–1121.
5. Nguyen PA, Groen AC, et al. (2014) Spatial organization of cytokinesis signaling reconstituted in a cell-free system. *Science* 346(6206):244–247.
6. Mitchison T, et al. (2012) Growth, interaction, and positioning of microtubule asters in extremely large vertebrate embryo cells. *Cytoskeleton (Hoboken)* 69(10):738–750.
7. Rappaport R (1996) *Cytokinesis in Animal Cells* (Cambridge University Press, Cambridge, UK).
8. Minc N, Burgess D, Chang F (2011) Influence of cell geometry on division-plane positioning. *Cell* 144(3):414–426.
9. Brinkley BR (1985) Microtubule organizing centers. *Annu Rev Cell Biol* 1:145–172.
10. Mitchison T, Kirschner M (1984) Dynamic instability of microtubule growth. *Nature* 312(5991):237–242.
11. Ishihara K, et al. (2014) Organization of early frog embryos by chemical waves emanating from centrosomes. *Philos Trans R Soc Lond B Biol Sci* 369(1650):369.
12. Field CM, Nguyen PA, Ishihara K, Groen AC, Mitchison TJ (2014) *Xenopus* egg cytoplasm with intact actin. *Methods Enzymol* 540:399–415.
13. Murray AW (1991) Cell cycle extracts. *Methods Cell Biol* 36(36):581–605.
14. Tsai M-Y, Zheng Y (2005) Aurora A kinase-coated beads function as microtubule-organizing centers and enhance RanGTP-induced spindle assembly. *Curr Biol* 15(23): 2156–2163.
15. Waterman-Storer C, et al. (2000) Microtubules remodel actomyosin networks in *Xenopus* egg extracts via two mechanisms of F-actin transport. *J Cell Biol* 150(2): 361–376.
16. Danuser G, Waterman-Storer CM (2006) Quantitative fluorescent speckle microscopy of cytoskeleton dynamics. *Annu Rev Biophys Biomol Struct* 35:361–387.
17. King SJ, Brown CL, Maier KC, Quintyne NJ, Schroer TA (2003) Analysis of the dynein-dynactin interaction in vitro and in vivo. *Mol Biol Cell* 14(12):5089–5097.
18. Tirnauer JS, Grego S, Salmon ED, Mitchison TJ (2002) EB1-microtubule interactions in *Xenopus* egg extracts: Role of EB1 in microtubule stabilization and mechanisms of targeting to microtubules. *Mol Biol Cell* 13(10):3614–3626.
19. Applegate KT, et al. (2011) plusTipTracker: Quantitative image analysis software for the measurement of microtubule dynamics. *J Struct Biol* 176(2):168–184.
20. Elinson RP, Rowning B (1988) A transient array of parallel microtubules in frog eggs: Potential tracks for a cytoplasmic rotation that specifies the dorso-ventral axis. *Dev Biol* 128(1):185–197.
21. Houliston E, Elinson RP (1991) Patterns of microtubule polymerization relating to cortical rotation in *Xenopus laevis* eggs. *Development* 112(1):107–117.
22. Vale RD (1991) Severing of stable microtubules by a mitotically activated protein in *Xenopus* egg extracts. *Cell* 64(4):827–839.
23. McNally FJ, Vale RD (1993) Identification of katanin, an ATPase that severs and disassembles stable microtubules. *Cell* 75(3):419–429.
24. Field CM, et al. (2011) Actin behavior in bulk cytoplasm is cell cycle regulated in early vertebrate embryos. *J Cell Sci* 124(Pt 12):2086–2095.
25. Verde F, Dogterom M, Stelzer E, Karsenti E, Leibler S (1992) Control of microtubule dynamics and length by cyclin A- and cyclin B-dependent kinases in *Xenopus* egg extracts. *J Cell Biol* 118(5):1097–1108.
26. Chang JB, Ferrell JE, Jr (2013) Mitotic trigger waves and the spatial coordination of the *Xenopus* cell cycle. *Nature* 500(7464):603–607.
27. Petry S, Groen AC, Ishihara K, Mitchison TJ, Vale RD (2013) Branching microtubule nucleation in *Xenopus* egg extracts mediated by augmin and TPX2. *Cell* 152(4): 768–777.
28. Clausen T, Ribbeck K (2007) Self-organization of anastral spindles by synergy of dynamic instability, autocatalytic microtubule production, and a spatial signaling gradient. *PLoS One* 2(2):e244.
29. Murata T, et al. (2005) Microtubule-dependent microtubule nucleation based on recruitment of gamma-tubulin in higher plants. *Nat Cell Biol* 7(10):961–968.
30. Goshima G, Mayer M, Zhang N, Stuurman N, Vale RD (2008) Augmin: A protein complex required for centrosome-independent microtubule generation within the spindle. *J Cell Biol* 181(3):421–429.
31. Petry S, Pugieux C, Nédélec FJ, Vale RD (2011) Augmin promotes meiotic spindle formation and bipolarity in *Xenopus* egg extracts. *Proc Natl Acad Sci USA* 108(35): 14473–14478.
32. Huang NP, Michel R, Voros J, Textor M, Hofer R (2001) Poly(l-lysine)-g-poly(ethylene glycol) layers on metal oxide surfaces: Surface-analytical characterization and resistance to serum and fibrinogen adsorption. *Langmuir* 17(2):489–498.
33. Tseng Q, et al. (2012) Spatial organization of the extracellular matrix regulates cell-cell junction positioning. *Proc Natl Acad Sci USA* 109(5):1506–1511.
34. Schneider CA, Rasband WS, Eliceiri KW (2012) NIH Image to ImageJ: 25 years of image analysis. *Nat Methods* 9(7):671–675.
35. Shivanandan A, Radenovic A, Sbalzarini IF (2013) MosaicIA: An ImageJ/Fiji plugin for spatial pattern and interaction analysis. *BMC Bioinformatics* 14:349.